Computers and Fluids 285 (2024) 106455

Contents lists available at ScienceDirect

Computers and Fluids

journal homepage: www.elsevier.com/locate/compfluid

Resolving subgrid-scale structures for multiphase flows using a filament moment-of-fluid method

Philippe Hergibo [a,b], Timothy N. Phillips [b], Zhihua Xie [a,*]

[a] School of Engineering, Cardiff University, Queen's Buildings, Cardiff, CF24 3AA, UK
[b] School of Mathematics, Cardiff University, Abacws, Cardiff, CF24 4AG, UK

ARTICLE INFO

Keywords:
Multiphase flow
MOF method
Filament capturing
Interface reconstruction
Subgrid-scale structure

ABSTRACT

Multiphase flows are present in many industrial and engineering applications as well as in some physical phenomena. Capturing the interface between the phases for complex flows is challenging and requires an accurate method, especially to resolve fine-scale structures. The moment-of-fluid (MOF) method improves drastically the accuracy of interface reconstruction compared to previous geometrical methods. Instead of refining the mesh to capture increased levels of detail, the MOF method, which uses zeroth and first moments as well as a conglomeration algorithm, enables subgrid structures such as filaments to be captured at a small extra cost. Coupled to a finite volume Navier–Stokes solver, the MOF method has been tested on a fixed grid and validated using well-known benchmark problems such as dam break flows, the Rayleigh–Taylor and Kelvin–Helmholtz instability problems, and a rising bubble. The ability of the novel filament MOF method to capture the filamentary structures that eventually form for the Rayleigh–Taylor instability and rising bubble problems is assessed. Good agreement has been found with other numerical results and experimental measurements available in the literature.

1. Introduction

Multiphase flow modelling plays a pivotal role in engineering since this class of flows are ubiquitous in many natural and industrial applications. They arise in electronics cooling, volcanic eruptions, cloud formation, and chemical reactions in bubble columns and fluidised beds. Investigating and understanding these phenomena necessitates the development of innovative technologies, enhancing process efficiency, safety, and sustainability. Consequently, a comprehensive understanding of multiphase flows remains indispensable to provide an accurate prediction of complex topological change.

Focusing on recent advances, we explore the key challenges faced in accurately capturing intricate interfacial dynamics and complex flow phenomena. Several numerical methods have been developed over the years to represent interfaces in multiphase flows, such as the marker-and-cell [1], volume-of-fluid (VOF) [2,3], front-tracking [4], level set [5,6], phase field [7] and particle methods [8]. All of these methods possess advantages and disadvantages [9]. The desirable attributes of these methods include easy implementation, fast computation and exact mass conservation, whereas undesirable features include high complexity, diffusive discretisation and low accuracy.

Among the methods described above, VOF methods are used extensively due to their natural characteristics, such as maintaining mass conservation, computational efficiency, and ease of implementation. In this context, two categories of algorithms exist for solving the transport equation for volume fraction: geometric and algebraic computation [3]. In the first category [9], interfaces are reconstructed based on volume fraction data, leading to the derivation of a geometric shape that approximates the actual interface. Subsequently, changes in volume fraction are computed by integrating volume fluxes across cell boundaries. In contrast, algebraic computation algorithms capture the interface by solving the transport equation for volume fraction using a high-resolution scheme [10–12].

Regarded as an extension of the VOF method, the moment-of-fluid (MOF) technique is employed to capture the interface separating two distinct materials [13]. As for the VOF method, the MOF method is based on a mesh approach with the difference being that the centroid is transported in addition to the volume fraction in order to reconstruct an interface solely within a cell, irrespective of neighbouring cells [13–16]. It has been shown that cells of any geometrical form can be used and the technique is not limited to a Cartesian grid. The process of transport and reconstruction of interfaces can prove to be computationally expensive since it relies on the efficiency of an optimisation procedure. However, recent developments have significantly reduced

* Corresponding author.
E-mail address: zxie@cardiff.ac.uk (Z. Xie).

https://doi.org/10.1016/j.compfluid.2024.106455
Received 21 April 2024; Received in revised form 8 October 2024; Accepted 12 October 2024
Available online 22 October 2024

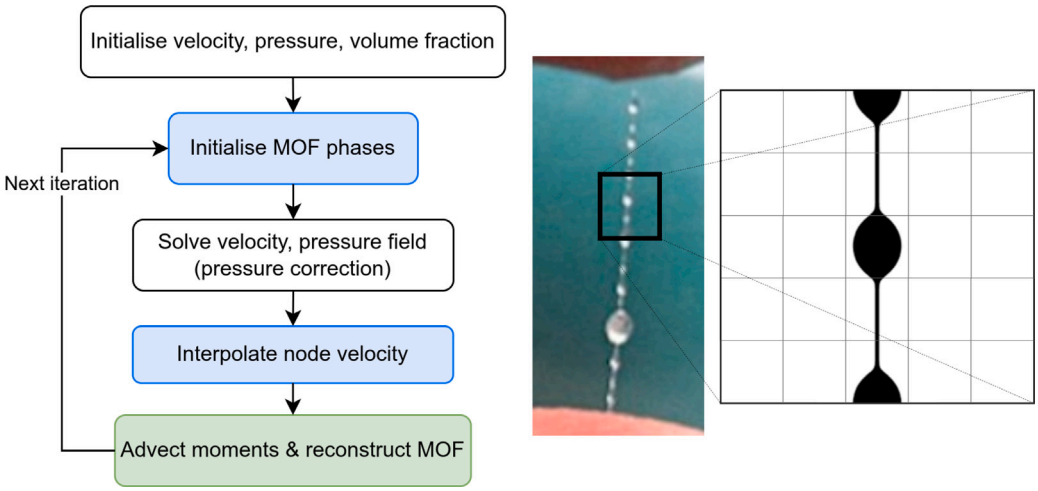

Fig. 1. Flowchart highlighting in blue the extra steps needed for the MOF method based multiphase flow solver. In green, the MOF method can select a standard or filament MOF. On the right hand side, subgrid structures are highlighted on a mesh-based approach with the example of saliva beads.

the computational cost of this process [14,17,18]. Recently, enhancements have been made to the original MOF method [13] through the use of symmetric reconstruction [19], expanding its applicability to multi-material configurations [20,21]. Consequently, this enhancement has facilitated the reconstruction of filaments and subgrid-scale structures [16,22].

Numerous methods have been used to couple interface capturing/tracking methods to a fluid flow solver based on the Navier–Stokes equations [23–27]. However, there has only been a limited number of attempts at performing this coupling with a MOF method. The first contribution coupled the MOF method with a finite element method [28]. Other contributions have employed a coupled level set moment-of-fluid (CLSMOF) method with a Navier–Stokes solver on a Cartesian grid but using a split advection method for several 2D and 3D benchmark problems [15,29]. There are also some contributions that have used MOF in engineering applications [30–33]. The dynamics of interfacial flows can produce highly complex topological changes. Therefore, based on fixed meshes, a very fine mesh across the entire computational domain is required to capture the intricate interfacial details, resulting in significantly increased computational effort.

The motivation of this paper is to couple the new filament MOF method recently developed by Hergibo et al. [16] to a Navier–Stokes fluid flow solver and assess performance of the new method. In this context, the incorporation of subgrid-scale filaments (shown in Fig. 1 for example) within the MOF method constitutes a novel contribution to the simulation of multiphase flows. This innovative approach addresses the challenges of resolving subgrid-scale features and complex changes in topology. By introducing subgrid filaments, the MOF method enhances the representation of thin films and droplets, while operating on a relatively coarse computational grid. In order to capture fine details using a reasonable computational cost, the community would generally consider using alternative techniques such as adaptive mesh or high-order methods. Tackling subgrid solutions for multiphase flows has caught recent interests in the community to limit the computational cost. However, limited research has been performed to assess the precision of the numerical subgrid structures as well as their fidelity. The novel MOF-based fluid solver proposed in the present study significantly improves numerical accuracy and computational efficiency, expanding the range of applicability of the MOF method with increased fidelity. The flowchart in Fig. 1 highlights in blue the extra steps required to complete the coupling between the novel filament MOF method and the Navier–Stokes solver. The green box highlights the choice of selecting either a standard MOF or a filament MOF depending on different scenarios.

This paper is structured as follows. Section 2 describes the flow solver and governing equations as well as the MOF method including how filaments are reconstructed within a cell on a fixed grid. The coupling between the flow solver and the MOF method is introduced together with the treatment of boundary conditions. Section 3 presents numerical results and analysis of several benchmark problems for a standard MOF method. In Section 4, the results of the novel filament MOF method coupled to the Navier–Stokes solver are presented for two classical benchmark problems. Some concluding remarks are made in Section 5.

2. Governing equations and numerical methods

2.1. Navier–Stokes flow solver

The governing equations are based on the Navier–Stokes equations. These are used for incompressible immiscible Newtonian two-phase flow. The continuity and momentum equations are, respectively, written in the form

$$\nabla \cdot \mathbf{u} = 0 \tag{1}$$

$$\frac{\partial(\rho \mathbf{u})}{\partial t} + \nabla \cdot (\rho \mathbf{u} \otimes \mathbf{u}) = -\nabla p + \nabla \cdot \left[\mu \left(\nabla \mathbf{u} + \nabla \mathbf{u}^T\right)\right] + \rho \mathbf{g} + \mathbf{f} \tag{2}$$

where $\mathbf{u}$ is the velocity vector, p is the pressure, $\mathbf{g}$ is gravity vector, $\mathbf{f}$ is the external forces vector and t is time. The fluid parameters, ρ and μ are the density and dynamic viscosity, respectively.

In terms of physical properties, the flow solver is constituted of relations for density and dynamic viscosity. These properties are defined by:

$$\rho = F\rho^a + (1 - F)\rho^b, \tag{3}$$

$$\mu = F\mu^a + (1 - F)\mu^b, \tag{4}$$

respectively, where the two fluids are labelled ‘a’ and ‘b’ and F denotes the volume fraction of material ‘a’ within a cell.

There are different discretisation methods for solving the governing equations, such as the finite difference method, finite volume method and finite element method [34]. In the context of the VOF method and its extension, a Cartesian grid is very favourable, hence the choice of the finite volume method due to its advantage for mass conservation.

A Cartesian grid based fluid flow solver is used for the computations. The governing equations are discretised using the finite volume method on a staggered Cartesian grid. The advection terms are discretised using a high-resolution scheme [35], combining high-order accuracy with

monotonicity, whereas the gradients in the pressure and diffusion terms are obtained using a central difference scheme. The SIMPLE algorithm is employed in the present study for the pressure–velocity coupling and a first-order backward Euler method is used for the time derivative. The pressure correction method is a numerical technique utilised in fluid dynamics simulations to enforce the satisfaction of the continuity equation in the context of incompressible flows. It involves computing an intermediate velocity field that may not initially satisfy mass conservation, followed by solving a pressure correction equation iteratively until the mass conservation requirement is satisfied to an acceptable level and a prescribed convergence criterion is met. The multiphase flow solver has already been extensively verified and validated through numerous test cases for flow over complex geometries [36], moving bodies [24], and fluid–structure interaction problems [37].

2.2. Surface tension model

In situations where interfacial forces are important, surface tension cannot be neglected. A continuum surface force (CSF) model is included in the Navier–Stokes equations to account for the surface tension. This force can be expressed as:

$$\mathbf{f}_{\text{CSF}} = \sigma\kappa\mathbf{n}\delta \tag{5}$$

where σ is the surface tension coefficient, $\mathbf{n}$ is the interface normal, $\kappa = -\nabla\cdot\mathbf{n}$ is the interfacial curvature and δ is the Dirac delta function. We use $\delta = |\nabla F|$ and $\mathbf{n} = \frac{\nabla F}{|\nabla F|}$ to address the surface tension modelling as a function of the volume fraction.

The interfacial normal $\mathbf{n}$ is discretised based on the smoothed volume fraction. The curvature term is discretised using an approximation of the normal at cell faces and its surrounding neighbouring values. It can be expressed as :

$$\kappa_{i,j} = -\left(\frac{n^x_{i,j} - n^x_{i-1,j}}{dx} + \frac{n^y_{i,j} - n^y_{i,j-1}}{dy}\right) \tag{6}$$

where the superscripts x and y corresponds to the horizontal and vertical components of the normal, dx and dy represent the grid size in the horizontal and vertical directions, respectively.

2.3. Interface capturing

The transport of the interface is governed by an advection equation for the volume fraction F:

$$\frac{\partial F}{\partial t} + \mathbf{u}\cdot\nabla F = 0 \tag{7}$$

where $\mathbf{u}$ is the velocity field. The choice of the MOF method has emerged as a prominent research topic for several key reasons. Its improved interface capturing ability, reduced numerical diffusion compared to VOF techniques and problems involving sharp discontinuities or complex geometries make it appealing for multiphase flows challenges. In addition, as an extension of VOF methods, the intrinsic mass conservation properties offered are advantageous for these types of computational model. The latest research in MOF methods aims to enhance computational efficiency and expand their relevance towards real applications. Also, it aims to address challenges concerning accuracy, robustness and efficiency.

2.3.1. Standard MOF method

The MOF method is an optimisation problem in which the zeroth and first moments of a material are used to reconstruct the interface using a Piecewise Linear Interface Calculation (PLIC). While the zeroth moment acts as a constraint, the difference between the first moments of the reference interface and its reconstruction needs to be minimised in order to obtain the best approximation of the normal to the interface. The detailed calculation of the zeroth and first moments can be found in Hergibo et al. [16]. The objective function, $E_c(\mathbf{n})$, defined by

$$E_c(\mathbf{n}) = \left|\mathbf{x}_{ref} - \mathbf{x}_{act}(\mathbf{n})\right| \tag{8}$$

where the $\mathbf{x}_{ref}$ represents the reference centroid and $\mathbf{x}_{act}$ the reconstructed centroid, captures this minimisation process, with $\mathbf{n}$ representing the outward unit normal to the interface. For non-rectangular cells, any optimisation method can be employed. However, for rectangular cells like Cartesian cells, an analytical solution exists, eliminating the need for a minimisation algorithm [14]. This has proven to be a significant improvement in reducing the computational cost. In this paper, the work from Lemoine et al. [14] has been used for most standard MOF reconstructions and working within this framework to enhance precision in reconstruction, the decision is made to reconstruct the material in a cell that has the smallest volume fraction [14].

2.3.2. Filament MOF method

Filaments are complex topological formations that arise during the deformation of materials (shown in Fig. 1). Since they are typically smaller in size compared to grid cells, the standard MOF method fails to determine their precise structure accurately. When dealing with filaments, a cell contains two interfaces, one on each side of the filament structure. Consequently, two separate reconstructions are required to accurately depict the topology. This necessitates an additional step in the procedure, as the detection of the thin structure must precede its reconstruction. In order to understand the topology, the conglomeration algorithm identifies materials/polygons that have no adjacent sides to one another. The algorithm detects them, and then forms two or more separate conglomerates. This study intelligently saves computational resources by limiting the number of conglomerates to two per material, with one of these considered to be a fictitious material. Note the detection is independent of the cell geometry.

When filaments are involved, a multi-material approach becomes necessary due to the creation of fictitious material. A nested dissection algorithm coupled to symmetric reconstruction techniques is employed, which minimises the number of conglomerates that are considered [19]. This not only reduces the computational complexity but also diminishes the number of combinations, resulting in improved efficiency [16]. The objective function, $E_c^{sym}(\mathbf{n})$, in a symmetric reconstruction process is given by

$$E_c^{sym}(\mathbf{n}) = \left|\mathbf{x}_{ref} - \mathbf{x}_{act}(\mathbf{n})\right| + \left|\mathbf{x}^{rem}_{ref} - \mathbf{x}^{rem}_{act}(\mathbf{n})\right| \tag{9}$$

where the superscript *rem* denotes the remaining conglomerates in a cell. Fig. 2 depicts the two MOF reconstruction approaches. The reference interface and its reconstruction are shown for a standard reconstruction. The centroid of the material considered as well as the centroid of the remaining material are highlighted to explain the symmetric MOF reconstruction. The filament reconstruction is shown with two conglomerates highlighted using dashed blue lines and their respective centroids in green. Note that in the filament case, two materials are grouped together and their volume fraction and centroid recalculated in this operation.

2.3.3. Material advection

The process of material advection encompasses the dynamic evolution of a material through translation, rotation, and deformation. Understanding these processes is crucial for evaluating the accuracy of interfacial methods. A purely Lagrangian approach is employed here, distinguishing it from other studies. This approach offers several advantages, including greater flexibility in choosing the Courant–Friedrichs–Lewy (CFL) number and an unsplit advection technique that employs a Lagrangian pre-image to capture the volume fraction and centroid of the material from the previous time step.

To achieve this, the vertices of a cell are traced backward in time using a second-order Runge–Kutta scheme (RK2) before determining the intersection between the pre-image and the material. This is a pragmatic decision which balances accuracy and computational expense compared with an approach that solely focuses on varying higher order schemes. Subsequently, forward advection is performed

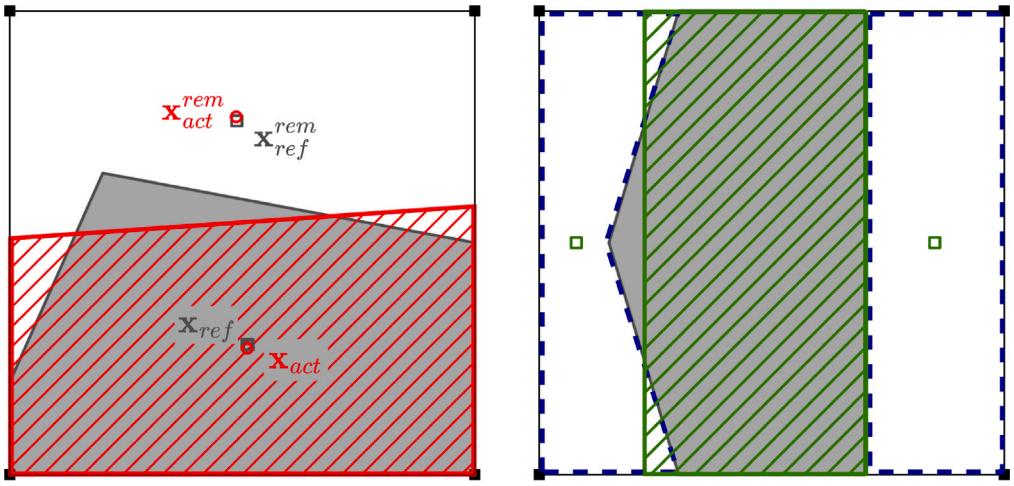

(a) Standard MOF (b) Filament MOF

Fig. 2. Schematic of the MOF reconstruction for both standard (a) and filament (b) methods. The reference interface is depicted in grey and its reconstruction in red for a standard MOF method. Filament reconstruction is highlighted in green with green squares denoting the reference centroid of conglomerates with a dashed blue line surrounding the desired material.

for centroids, and reconstruction is conducted using the corresponding volume fraction.

When enabling the filament MOF reconstruction in a simulation, additional steps are required to ensure the advection process is complete. While the standard MOF can be performed only using the desired material as targeted intersection, the filament MOF needs to intersect all materials present in the domain in order to reproduce the exact topology. Moreover, the conglomeration algorithm, which also contains the adjacency test, is performed which enables the volume fraction and centroid of conglomerates to be calculated. Only then, can the choice between standard MOF and filament MOF be made. Fig. 3 summarises the essential steps involved in the advection process for both standard and filament MOF.

These advection procedures are valid for a single cell reconstruction. However, there are two important aspects of these procedures that are not discussed here, viz. the limitation to three materials for filament MOF and the redistribution algorithm or repair to conserve mass/volume fraction through the time iterations. Details of these can be found in the recent work of Hergibo et al. [16].

2.4. Boundary conditions

To fully specify the mathematical model, it is imperative to establish boundary conditions that play a critical role in defining fluid flow behaviour at the boundaries of a finite computational domain. They accurately capture the interaction between the fluid and its surroundings, classified into inflow, outflow, and solid boundaries. Inflow conditions specify fluid characteristics upon entering the domain, while outflow conditions prevent disturbances caused by fluid leaving the domain. Solid boundaries simulate fluid interactions with solid objects through various approaches. Accurate selection and implementation of boundary conditions are crucial for reliable results in numerical fluid simulations, requiring careful consideration of the specific problem and desired representation of fluid behaviour near the boundaries.

In most MOF methods, the treatment of the boundary condition is rarely discussed as the interfacial topology is inside the computational domain. However, the reduction of the number of neighbouring cells near the boundary means that MOF methods exhibit better accuracy when reconstructing interfaces in these regions. Therefore, special attention needs to be paid to the MOF method in addition to the boundary conditions for the Navier–Stokes solver.

2.5. Coupling between flow solver and MOF method

While the MOF method presented above uses node velocities during the advection process [16], in both x and y-directions, the finite volume Navier–Stokes flow solver uses face velocities [35]. To accommodate this, an extra step is needed to interpolate the node velocity before MOF advection can be performed. The face velocity, representing the velocity at the face of each control volume, is commonly known and readily available. However, to compute the node velocity, which characterises the velocity at the corner of each control volumes, a simple linear interpolation technique is employed. Note that for each control volume, the east face defines the x-velocity, the north face defines the y-velocity, whereas the bottom left node defines both x and y-velocities simultaneously (see Fig. 4).

The case of a control volume located next to a wall is illustrated in Fig. 5. When dealing with boundary conditions, additional adjustments are required to ensure proper treatment of the velocity field near the boundaries. The interpolated node velocities near the boundaries are adjusted to adhere to the prescribed boundary conditions, maintaining consistency with the physics of the problem. For no-slip conditions, the interpolated velocities at the wall are zero. In this instance, the node velocity at the wall in the tangential direction is forced to take the value at its nearest node, typically the first node velocity in its normal direction. It is interesting to note that this can be overcome by using a slip condition for the MOF method. Regarding periodic boundary conditions, node velocities remain unaffected by the domain boundaries. Nevertheless, the use of ghost cells presents a counter-intuitive aspect. Regardless of the direction of periodicity, the first row/column of cells corresponds to the last row/column of cells in the domain. In this instance, the row/column of ghost cells on one side corresponds to the penultimate row/column of cells of the domain of the opposite side and vice versa.

Mass conservation is performed only near the interface. Indeed, in order to reduce computational expense, only cells near the interface are advected as the CFL constraint guarantees that cells further away from the interface maintain their volume fraction. Therefore, material distribution is performed on “mixed” cells, i.e. cells that contain an interface in a global fashion. Over/under-filled cells are used to redistribute mass uniformly to mixed cells in the domain. More details on the redistribution procedure can be found in [38]. The authors are aware that this does not guarantee mass conservation to machine precision. However, the choice of time step may influence mass variation during the simulation, which is not discussed in the remainder of this paper.

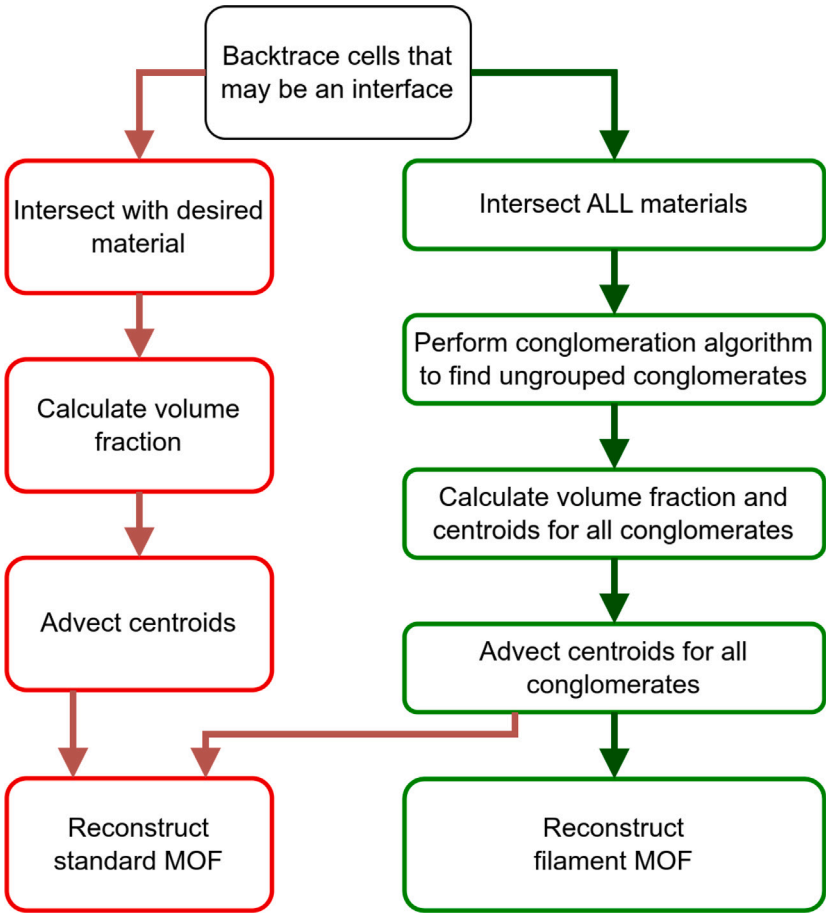

Fig. 3. Flowchart highlighting key steps to standard and filament MOF reconstruction and advection. Red denotes the use of standard MOF. Green denotes the use of filament MOF.

3. Results

In this section, the coupling between a flow solver and our MOF method is validated. We present results obtained from the numerical simulations using the MOF method for simulating multiphase flows. The filament capability is enabled for this series of simulations. This implies that if the topology does not produce thin structures, the reconstruction will remain standard. The simulations were performed on a two-dimensional domain using a Cartesian grid in order to validate our numerical implementation by considering well-known benchmark test cases.

In our previous publication dedicated to pure advection problems, both standard MOF and filament MOF methods have shown good agreement on test cases where a prescribed divergence-free velocity field is imposed [16]. In the present study, these methods are applied to dynamic physical test cases where the velocity field is determined by solving the momentum equation and will not be identically divergence-free due to numerical rounding errors.

3.1. Dam break

We examine the classical benchmark 2D dam break flow problem, that has been investigated extensively both experimentally [39] and numerically [40]. The computational domain has dimensions of $4a \times 4a$ in the streamwise and vertical directions, respectively. Initially, a water column of height $2a$ and width a is at rest. In this study we choose $a = 0.146$ m. Three computational grids are used, 32×32, 64×64, 128×128, respectively.

Fig. 6 displays snapshots of the computed remaining water interface for a coarse mesh. Note that the leading edge of the water column swirls into a small recirculation region that is captured by the accurate MOF method. Physically, the surge front and height position are good indicators of high-fidelity simulations. These can be compared with experiments. In terms of surge position, since the dam cannot be instantly removed in the experiment, a slight time delay in the experimental data is expected, which is also observed in other numerical simulations. A delay of 0.27 in nondimensional units is observed, which corresponds to 0.023 s. Fig. 7 shows the comparison between our simulations using several meshes with the VOF simulations of Xie & Stoesser [24] and experiments of Martin [39]. Generally, the numerical results converge as the mesh is refined, with only a minor disparity in surge position between the coarse and fine mesh simulations.

In order to investigate the convergence rate of the present method further, the free surface profiles obtained from the simulations on the three meshes at $T = 1$ and $T = 2$ are compared to the benchmark solution. Additionally, an extra simulation using an even finer mesh of 256×256 is performed; the resulting air–water interface is considered as the benchmark solution for the purpose of the convergence study. Fig. 8 presents the calculated L_1, L_2, and L_{inf} errors in relation to the benchmark solution. The convergence rate is observed to lie between first-order and second-order, tending towards second-order as the fine mesh is approached. The surge position error shows similar trends. It is interesting to note the oscillation in mass variation during the simulation due to the advection of only the interface and redistribution procedures.

3.2. Rayleigh–Taylor instability

This well-known instability is a phenomenon that emerges when a gravitational field causes a heavy fluid initially at rest on top of a lighter

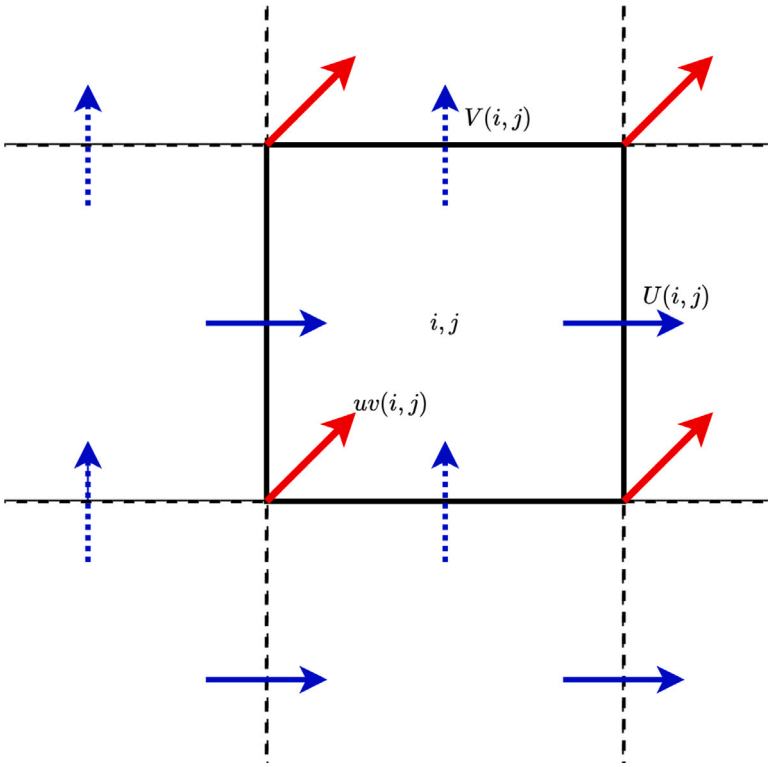

Fig. 4. Face velocities are defined at the face of the control volume. $U(i,j)$ denotes the horizontal velocity of cell i,j in full blue arrow. $V(i,j)$ denotes the vertical velocity of cell i,j in dashed blue arrow. Node velocity is interpolated from two neighbouring control volumes (red arrows). $uv(i,j)$ denotes both horizontal and vertical velocities of cell i,j at the node.

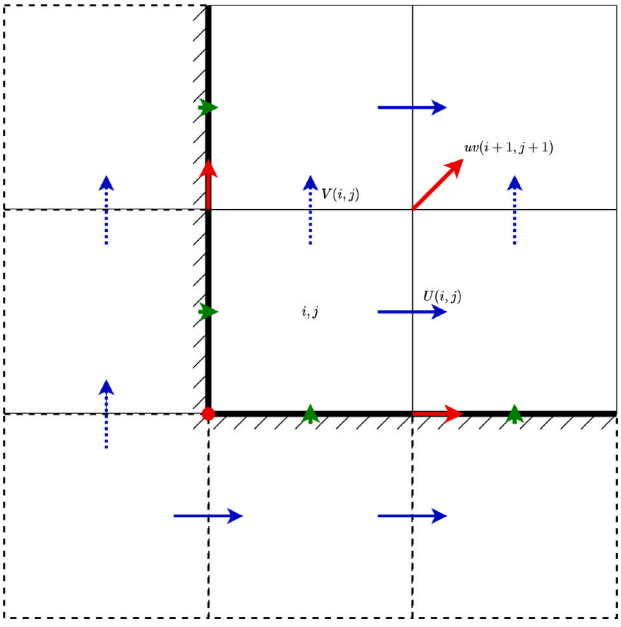

Fig. 5. Schematic diagram showing the wall boundary conditions imposed in the domain for all velocities at the bottom left edge of the domain. Cells in dashed lines are ghost cells. Red arrows and dot represent the node velocities for MOF treatment. Green arrows are imposed boundary conditions for face velocities.

fluid to deform the interface between them. In our study, we adopt the same configuration as previous investigations [23,25,26]. The rectangular domain is $[0,d]\times[0,4d]$. The Atwood ratio At, which signifies the density difference between the heavier and lighter fluids, is set to 0.5. Additionally, we set the Reynolds number $Re_A = \rho_A d^{3/2} g^{1/2}/\mu_A = 3000$, where ρ_A and ρ_B represent the densities of the heavier and lighter fluids, respectively, and μ_A corresponds to the dynamic viscosity of the heavier fluid. The interface between the two fluids is initially perturbed with a sinusoidal waveform of amplitude $0.1d$. Following Tryggvason's work [25], we employ non-dimensional variables, scaling length by d, time by $\sqrt{d/Atg}$, and velocity by $\sqrt{Atgd}$. Surface tension is not considered.

We conduct computations using three fixed Cartesian meshes, 32×128, 64×256 and 128×512, respectively. Fig. 9 highlights the different stages of the deformation of the interface from a non-dimensional time $T = 0$ to $T = 2$. We observe that the vortex formed during the spike penetration is well reconstructed. The interface remains sharp and does not exhibit any diffusion.

The predictions of the present numerical scheme for this test case are compared to those of other methods in order to ensure the correct behaviour is achieved. Fig. 10 shows the position of the perturbation for both the heavy and light fluid. Good agreement is found with other methods for both fluids [23,25]. Whilst the position of the perturbation is a good criterion to ensure that the physics is correctly captured, the precision of the vortex is also a good criterion. However, the vortex is reconstructed more precisely with finer meshes. We believe that grid convergence is not appropriate for this test case. Instead, the spike penetration position and its error relative to a benchmark solution on the finest mesh are more appropriate measures of the accuracy of the approximation.

In this instance, the benchmark considered is the solution on a 256×1024 grid. The error corresponds to the distance of the spike position relative to the benchmark solution. The convergence is then evaluated for each grid. Fig. 11 highlights that near quadratic convergence is obtained. In addition, the mass loss during the evolution of the flow is kept to within 0.2%. A sudden loss of mass occurs at the beginning when the interface evolves slowly.

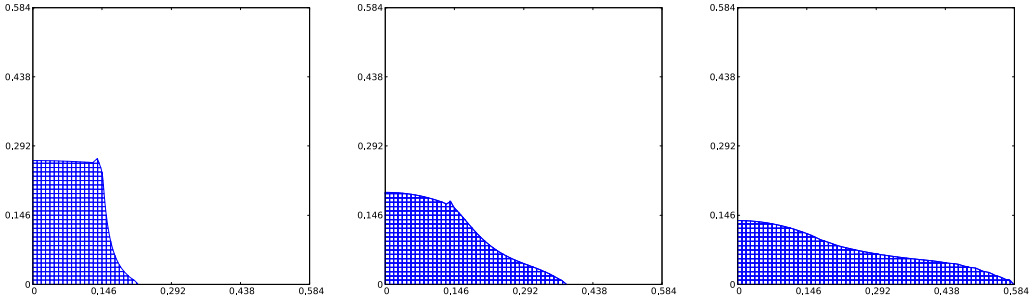

(a) $T = 1$ (b) $T = 2$ (c) $T = 3$

Fig. 6. Snapshots of the interface for the dam break test case for a 64 × 64 grid.

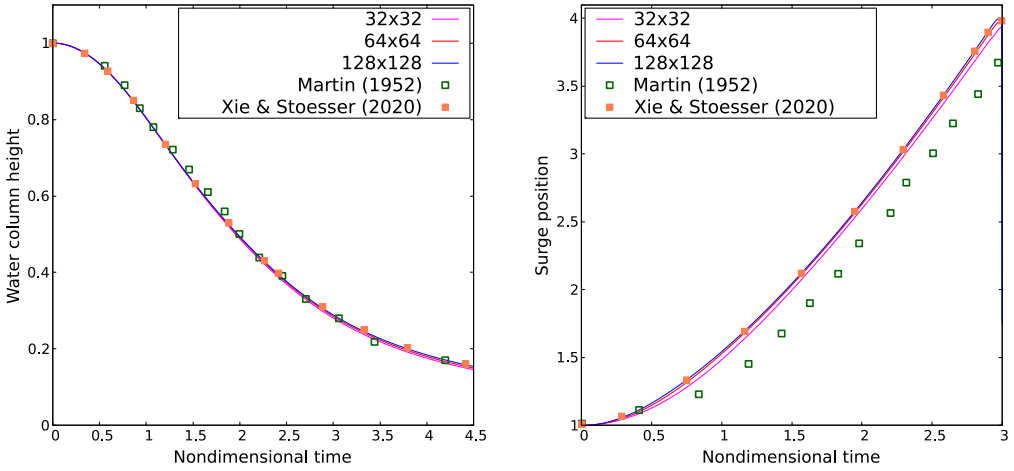

(a) Water column height (b) Surge front position

Fig. 7. Convergence of (a) water column height, and (b) surge front position, with mesh refinement and comparison with the numerical predictions of Xie and Stoesser [24] and the experimental data of Martin [39].

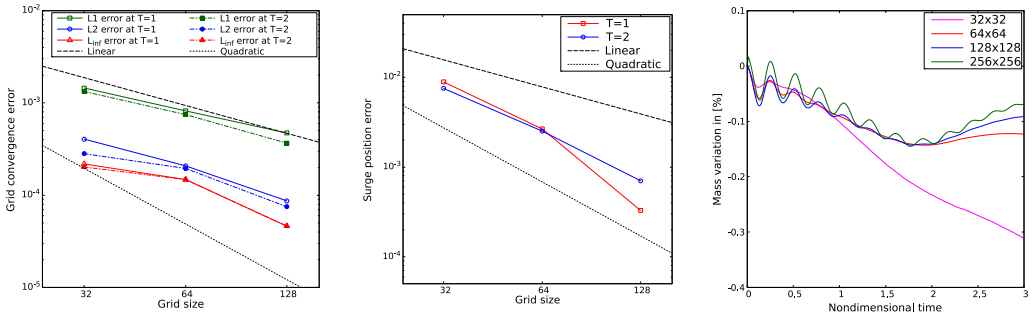

(a) Grid convergence (b) Surge position convergence (c) Mass variation

Fig. 8. Convergence study for the dam break case, using grid convergence and surge position convergence as well as mass variation.

3.3. Kelvin–Helmholtz instability

This well-known instability is a phenomenon that occurs when fluids with different velocities interact. It is formed due to the shearing motion between fluids, leading to the formation of vortices. It is commonly observed in natural settings such as cloud formations, ocean currents, and atmospheric phenomena like jet streams. The domain of ratio $4 : 1$ contains two fluids of the same densities and viscosities. Gravity is neglected. At the initial stage, the interface between the two fluids takes the form of a sinusoidal function $0.5(1 + 0.01\sin(2\pi x))$. The fluid at the bottom has a velocity of amplitude 0.5 towards the left hand side of the domain. The fluid at the top has a velocity of amplitude 0.5 towards the right hand side of the domain in order to create the shear motion. Periodic boundary conditions are employed in the horizontal direction, while no-slip wall boundary conditions are imposed on top and bottom boundaries.

Numerical predictions for this test case are performed for two different grid sizes, respectively 128×32 and 256×64. Fig. 12 shows snapshots of the evolution of the interface at $t = 0$ s, $t = 1$ s, $t = 2$ s and $t = 3$ s, respectively, in physical time. The vortices are well reconstructed. Note that even for a coarse mesh, the gap between the

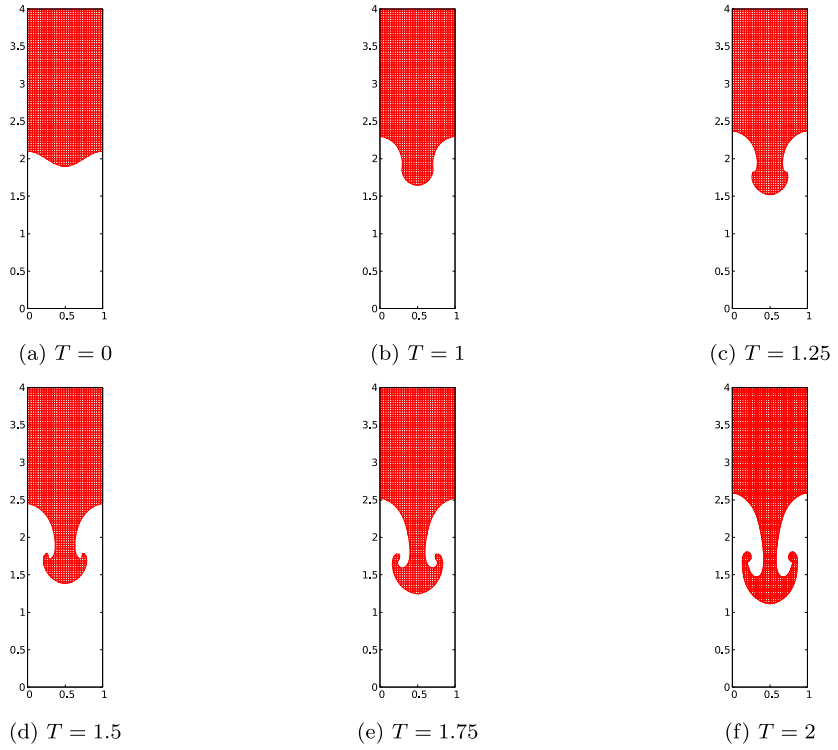

(a) $T = 0$ (b) $T = 1$ (c) $T = 1.25$

(d) $T = 1.5$ (e) $T = 1.75$ (f) $T = 2$

Fig. 9. Evolution of the Rayleigh–Taylor instability interface using the standard MOF method for a 32×128 grid.

two fluids remains larger than a cell size, which justifies the decision not to use a filament MOF method for this test case.

4. Filament MOF method coupled with Navier–Stokes equations

4.1. Rayleigh–Taylor instability

In this section, we discuss the coupling between a flow solver and our filament MOF method. Resolving subgrid-scale structures for multiphase flows is challenging. It requires an extremely accurate method. Our newly developed filament MOF method [16] is one such method that possesses good reconstruction features mainly for filamentary flows. The Rayleigh–Taylor instability problem exhibits these characteristics. However, most numerical techniques for this benchmark problem are unable to resolve these filamentary structures and are limited to simulation times before the development of thin structures. On the one hand, finer grids are used to resolve fully the physical phenomena occurring in these instances. On the other hand, if coarser meshes are used, unphysical filament break-ups would likely arise. In this section, we show some results illustrating the coupling between the filament MOF method and the finite volume Navier–Stokes solver.

Fig. 13 shows snapshots of the Rayleigh–Taylor instability problem at a non-dimensional time of $T = 3$ for three different grids, 32×128, 64×256 and 128×512, respectively. The black rectangle denotes the area where zoomed solution is provided. Note that the filament solution seems to be reconstructing filaments in a reasonable fashion. Filament breakups are reduced drastically, although they may still occur. In addition, at this later non-dimensional time, here $T = 3$, the different grids do not seem to overlap, reducing any chance of grid convergence study. The finer grid shows an asymmetry in the lighter fluid position. This may be due to different dynamic rather than gravitational buoyancy occurring in the wake generation.

However, the physical spike penetration position remains a good quantity to evaluate. Fig. 14 highlights the position of the heavy and light fluid during the simulation. In this case, the non-dimensional time has been extended to $T = 3$. Note the heavy fluid spike position

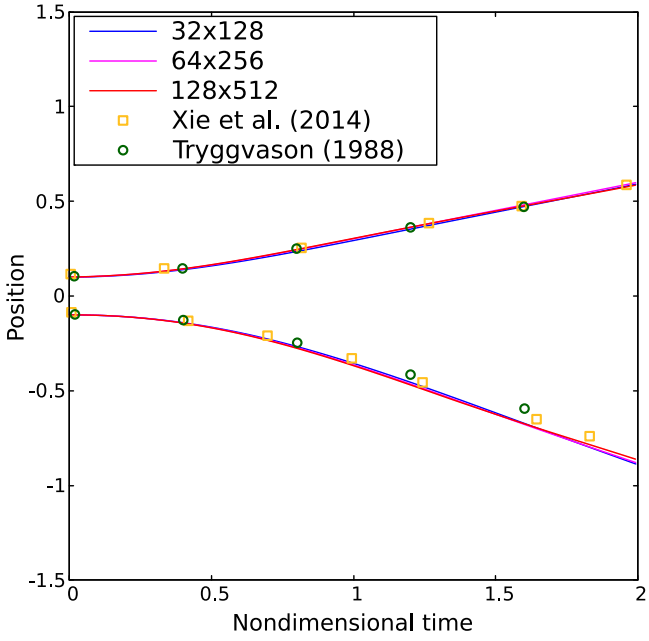

Fig. 10. Evolution of the position of the heavier and lighter fluids in nondimensional units.

continues to go downwards and even seems to accelerate at these later stages. To the best of the authors' knowledge, no comparison can be made for physical spike position at later stages. As to mass variation, it shows a similar trend to the standard MOF results showed above. A maximum of 0.654% mass loss is reached at $T = 3$ for the coarsest mesh 32×128.

As a comparison, Fig. 15 shows the exact comparison between the standard MOF and the filament MOF method. We observe that despite the filaments not being resolved appropriately, the standard

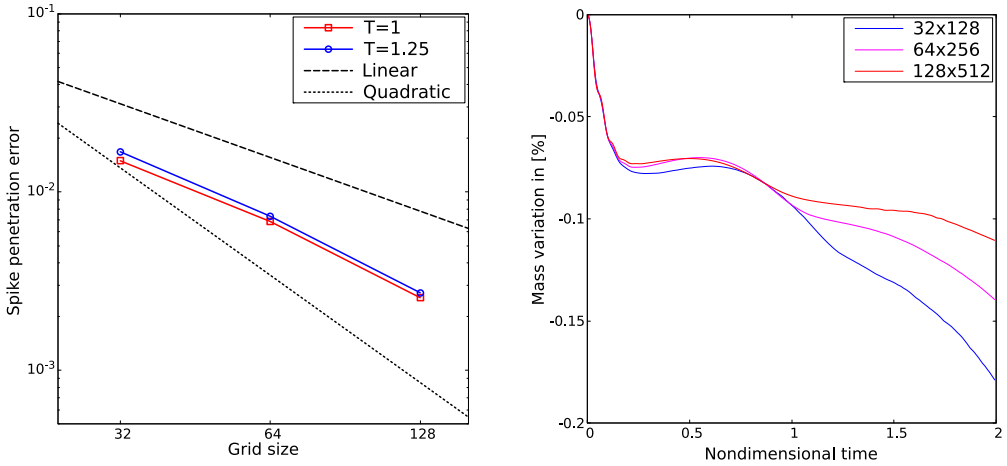

(a) Spike penetration error (b) Mass variation

Fig. 11. Convergence study on the Rayleigh–Taylor case, using spike penetration error convergence as well as mass variation.

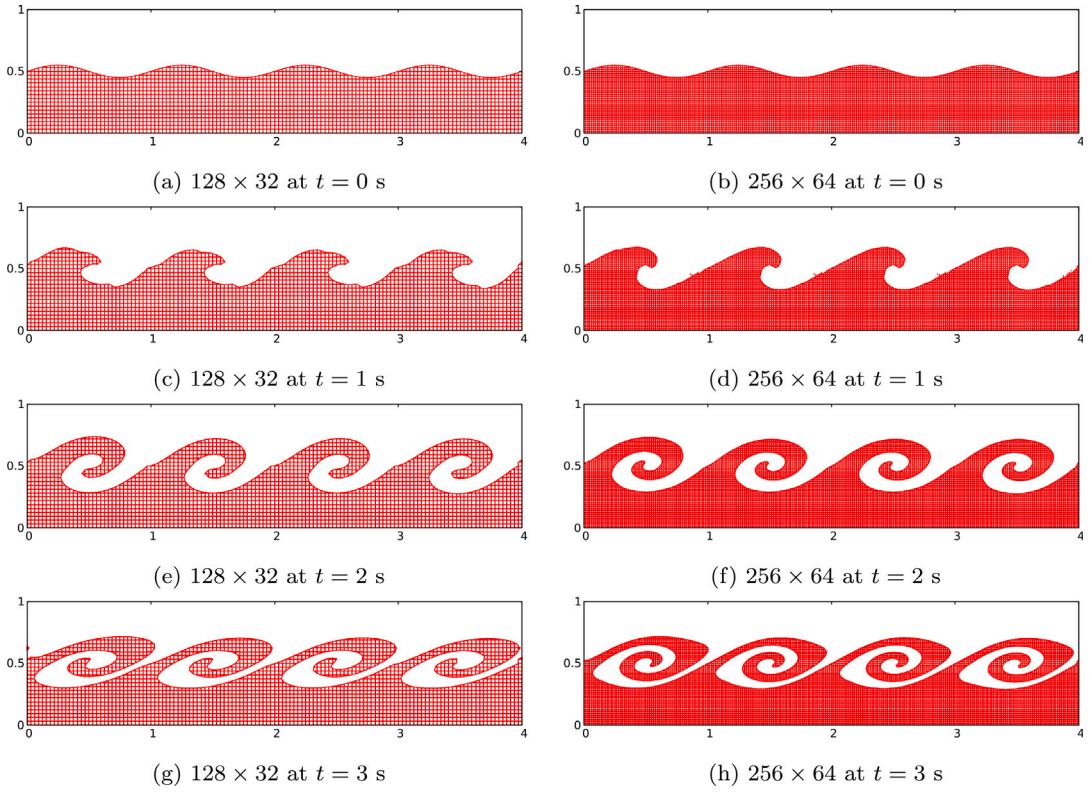

(a) 128×32 at $t = 0$ s (b) 256×64 at $t = 0$ s

(c) 128×32 at $t = 1$ s (d) 256×64 at $t = 1$ s

(e) 128×32 at $t = 2$ s (f) 256×64 at $t = 2$ s

(g) 128×32 at $t = 3$ s (h) 256×64 at $t = 3$ s

Fig. 12. Snapshots of the Kelvin–Helmholtz instability interface using the MOF method on 128×32 (left) and 256×64 (right) grids.

MOF cannot resolve any feature that is thinner than a cell size. The standard MOF simulation exhibits unphysical breakups. As subgrid-scale structures get resolved more accurately, effort needs to be made to ensure that the solution is physical and is validated with high-fidelity numerical simulations. Quantifying features of the mushroom shaped tail would be an interesting addition to the community.

Runtime is also compared between the standard and filament MOF methods. On a single core, the test case takes 27 s to run for a standard MOF simulation, whereas the filament MOF simulation takes 38 s. As expected, understanding the topology through the conglomeration algorithm and performing filament reconstruction is more expensive. However, a 40% increase in runtime is not significant when taking into consideration the quality of the reconstruction. Once filaments break up, coalescence is not possible for this case. This leaves the user with a choice of balance between fast runtime and accuracy in reconstruction.

4.2. 2D rising bubble case

In this section, we consider a second benchmark problem, the 2D rising bubble problem, in which filament structures are created. In this problem a bubble of radius $r = 0.25$ is initially positioned with its centre at the point $(0.5, 0.5)$ in the rectangular domain $[0, 1] \times [0, 2]$. Slip boundary conditions are applied at the left and right walls, and no-slip conditions are imposed on the top and bottom walls. Following Hysing et al. [41], we study the case in which thin trailing filaments are created due to surface tension. The density ratio between liquid and gas phase

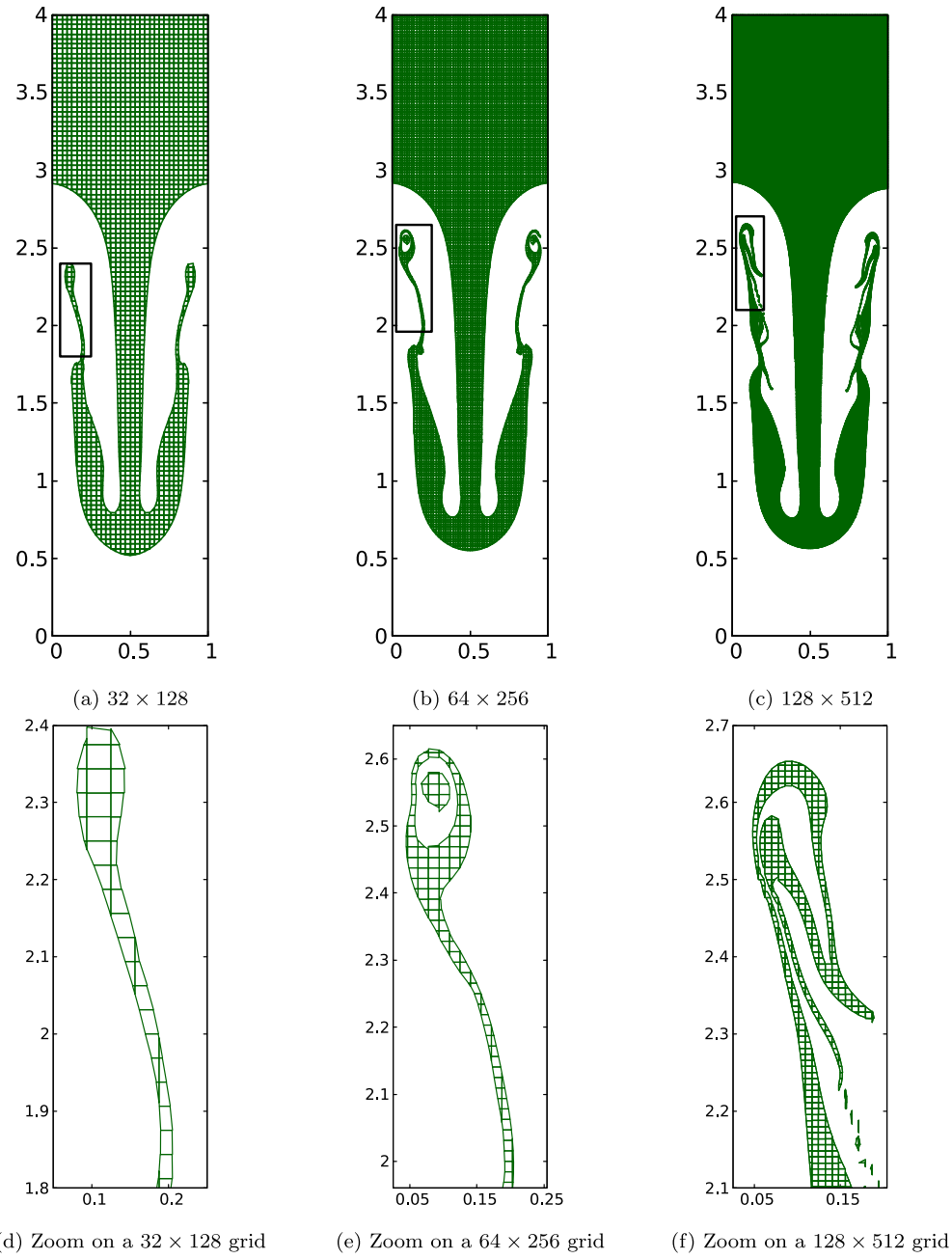

(a) 32 × 128 (b) 64 × 256 (c) 128 × 512

(d) Zoom on a 32 × 128 grid (e) Zoom on a 64 × 256 grid (f) Zoom on a 128 × 512 grid

Fig. 13. Snapshots of the Rayleigh–Taylor instability interface using the filament MOF method at $T = 3$. Black rectangle highlights zoomed in areas on the top row. Bottom row shows zoomed in areas.

is 1000, whilst the viscosity ratio is 100. The surface tension coefficient is 1.96 N m^{-1} and the acceleration due to gravity is 0.98 ms^{-2}. Surface tension is modelled through an additional term in the external force balance as discussed in Section 2.2.

This study involves three Cartesian grid resolutions, 30 × 60, 60 × 120 and 120 × 240. The simulation is run until $t = 3$ s. Fig. 16 shows the visual representation of the shape of the bubble at the final stage. The bubble develops filaments as it rises which breaks up under the action of surface tension. Possible causes of filament break up include the numerical treatment of filamentary structures, calculation of the curvature of the bubble surface or the time stepping procedure.

Fig. 17(a) compares the bubble profile on the finest grid at $t = 3$ s with the corresponding profiles generated in the literature [41,42]. Both references use a finite element method. The numerical results show that the trailing filament is resolved differently. We can see a clear breakup for the TP2D (Transport Phenomena in 2D) method whereas the conservative level-set method of Doherty et al. [42] manages to maintain the satellite bubble within the main bubble. We also note that we predict a slightly larger bubble elevation which may be caused by a slightly larger rise velocity or a larger overall volume resulting in a greater buoyancy force. One of these reasons may be dismissed with reference to the mass variation shown in Fig. 17(b). Indeed, the mass of the bubble varies throughout the numerical calculation but at the end of the calculation there is a negative variation suggesting a loss. The mass loss is maintained within a margin of 1% for the finest grid.

Another interesting analysis is to compare the shape of the bubble between the standard MOF and the filament MOF methods. As a comparison, Fig. 18 illustrates the exact comparison of bubble shapes at $t = 3$ s. Despite the filament MOF method exhibiting breakups due to large deformation, the standard MOF method cannot resolve any feature that is thinner than a cell size appropriately. The filament MOF method shows promising results for the rising bubble case.

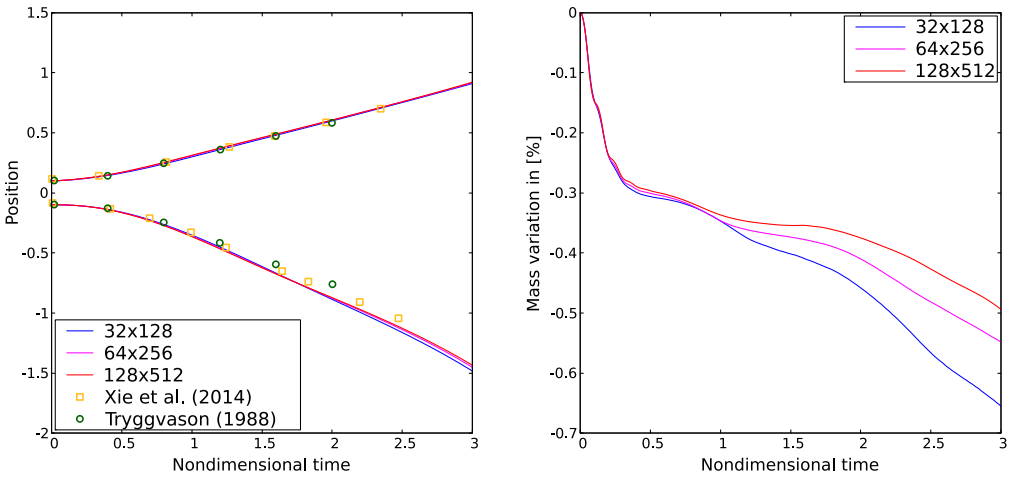

(a) Evolution of spike position compared to other methods

(b) Mass variation when using filament MOF

Fig. 14. Study on the Rayleigh–Taylor case using filament MOF. Spike penetration position (a) and mass variation (b) are presented.

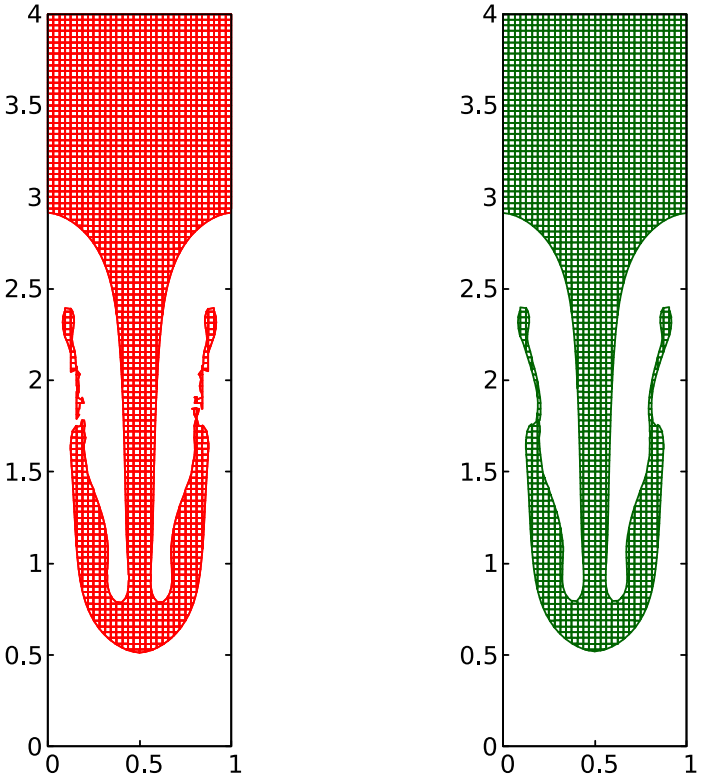

(a) Standard MOF
Runtime : 27 s

(b) Filament MOF
Runtime : 38 s

Fig. 15. Comparison of the standard (a) and filament (b) MOF method for the Rayleigh–Taylor instability problem at $T = 3$ for a 32×128 grid and their respective runtimes.

5. Conclusions

In this paper, the filament moment-of-fluid method coupled to a finite volume Navier–Stokes solver has been presented for multiphase flows on a fixed grid. First, the standard MOF is implemented for different benchmark test cases where the complexity of the flow is relatively low. Then, the filament MOF is introduced where subgrid-scale structures are resolved for a highly complex flow structure. This represents a significant advancement in the understanding and modelling of complex multiphase flows. Higher levels of accuracy and efficiency in capturing the intricate interactions between two phases are achieved. A direct comparison has shown the differences of approach between a standard MOF and a filament MOF. The representation of filaments is relatively well captured using the latter method, despite some remaining filament breakups. Promising results in resolving subgrid-scale structures have been demonstrated.

The proposed method is tested on well-known benchmark problems featuring different levels of complexity. Good quantitative predictions of the evolution of the water column height and position of the surge front are achieved with both experimental measurements and previous

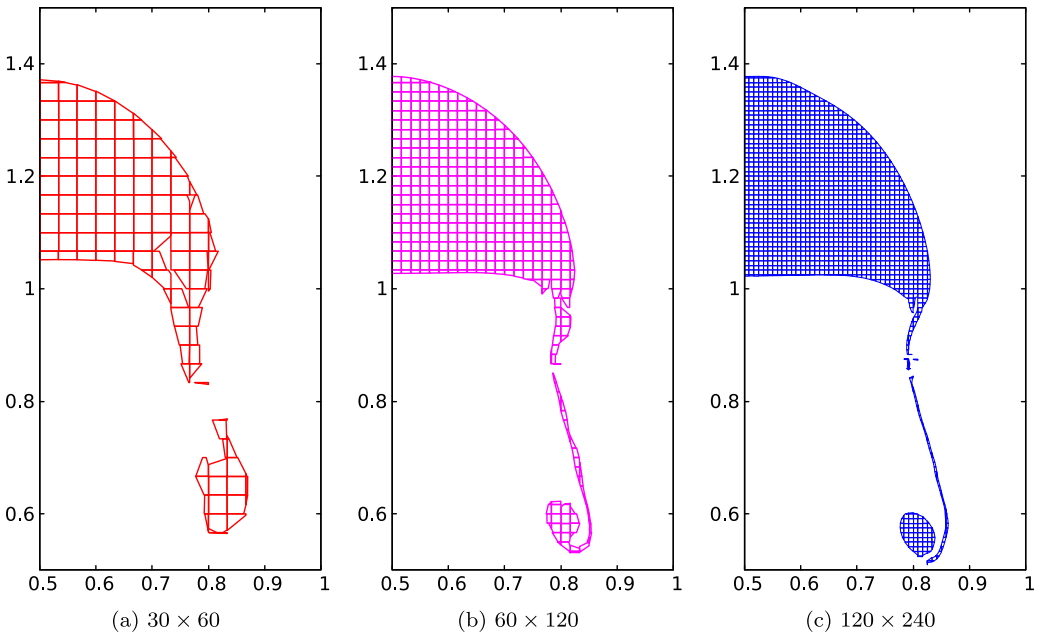

(a) 30×60 (b) 60×120 (c) 120×240

Fig. 16. Bubble profile at $t = 3$ s using filament MOF method for three different grid sizes.

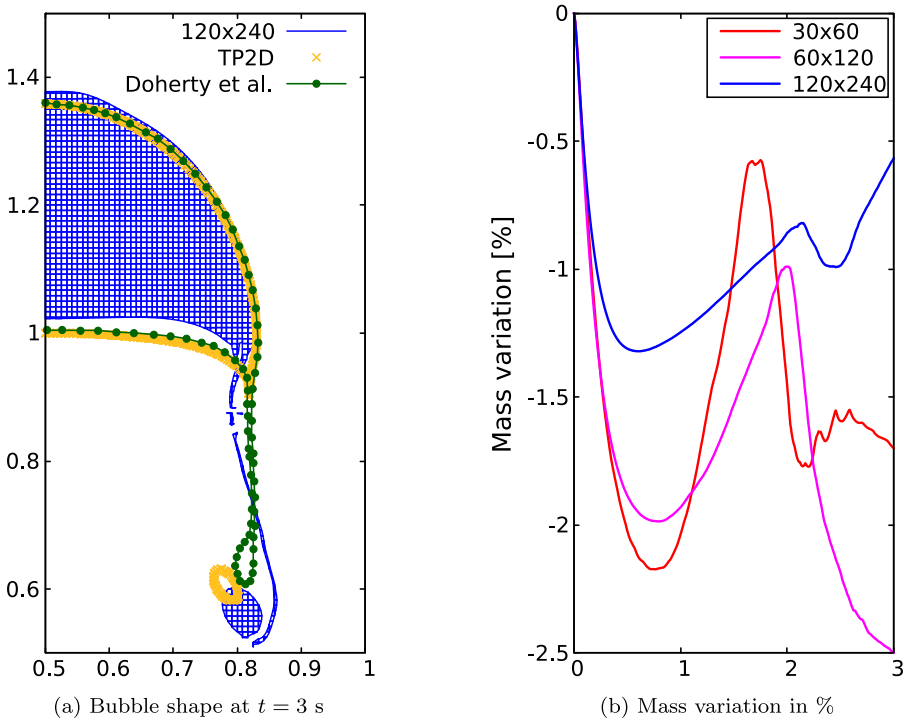

(a) Bubble shape at $t = 3$ s (b) Mass variation in %

Fig. 17. Comparison of the bubble shape at $t = 3$ s using filament MOF method with other references in the literature [41,42] for a 120×240 grid and its mass variation for the rising bubble case for different mesh resolutions.

numerical studies for the dam break flow problem. In the case of the Rayleigh–Taylor instability problem, the method is able to reconstruct the interface in a precise manner during the early stages of development, while the filament MOF preserves highly deformed subgrid-scale structures during the later stages. Both standard and filament MOF methods maintain satisfactory agreement with the predictions of other numerical methods. The method exhibits a good level of accuracy for the Kelvin–Helmholtz instability problem with qualitative agreement with other results in the literature and recent MOF methods. Finally, the rising bubble case, which exhibits filament structures, is tested using the filament MOF method including surface tension modelling. The filament does break up but the flow features are captured even for coarser grids. Qualitative results agree well with references using finite element methods in the literature.

Despite these advances, challenges remain in the material diffusion in interface capturing methods similar to MOF methods. Whether it is sharp edges or under-resolved structures such as a filament tip or tail, numerical simulations of multiphase flows with the moment-of-fluid method encounter difficulties in the reconstruction of these features. However, the method shows greater ability to reconstruct accurate interfaces in complex situations such as near boundaries or

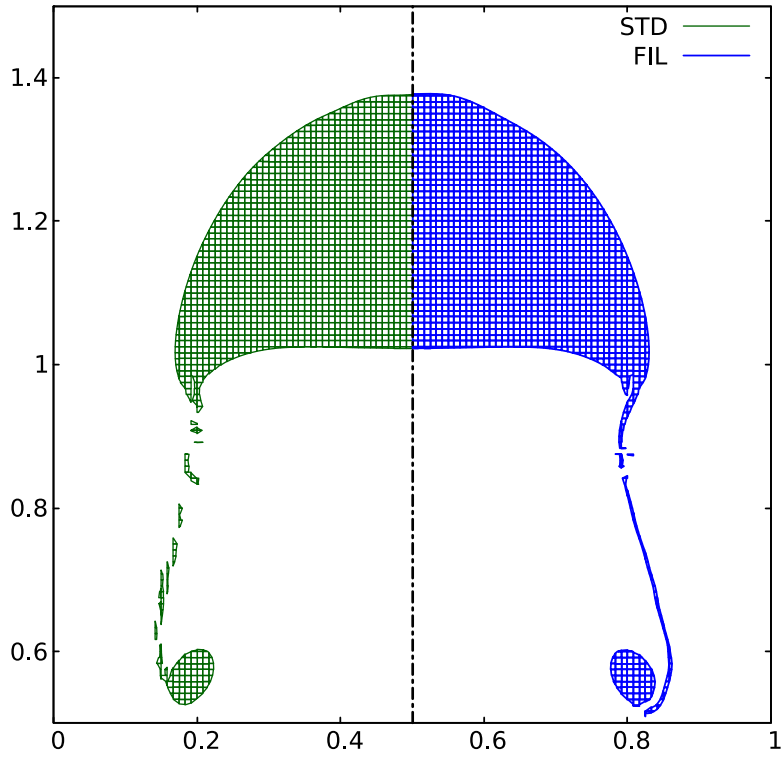

Fig. 18. Comparison of the bubble shape at $t = 3$ s between the standard MOF (left) and filament MOF (right) method for a 120 × 240 grid.

filament/multi-material over VOF and LVIRA methods. In addition, surface tension has been modelled in this paper and may need additional improvements to capture the numerical curvature more precisely. The complexity of the method and the associated computational cost, although mitigated with analytical solution on Cartesian grids, may be a limiting factor for its use. The MOF method can be also extended to other more general meshes, such as unstructured grids for example, although our focus is the Cartesian grid solver here, which can deal with complex geometries using the cut-cell method [36]. Nevertheless, the moment-of-fluid method remains a robust and promising improvement to interface capturing/tracking methods and in numerical multiphase flows in general. Increasing the levels of detail in subgrid-scale structure as well as including turbulence modelling, whether for Newtonian or non-Newtonian flows is our next priority while maintaining acceptable levels of computational resources. In addition, using adaptive mesh methods may be of interest. Addressing challenging 3D problems is also a development that we wish to pursue in the future. The moment-of-fluid method is an example of the next generation of interface capturing methods and will play an integral role in the analysis and prediction of complex multiphase systems.

CRediT authorship contribution statement

Philippe Hergibo: Writing – original draft, Visualization, Validation, Software, Methodology, Investigation, Formal analysis, Data curation. **Timothy N. Phillips:** Writing – review & editing, Supervision, Methodology, Investigation, Conceptualization. **Zhihua Xie:** Writing – review & editing, Supervision, Software, Methodology, Investigation, Funding acquisition, Conceptualization.

Declaration of competing interest

The authors declare that they have no known competing financial interests or personal relationships that could have appeared to influence the work reported in this paper.

Acknowledgements

Constructive comments from anonymous reviewers have helped to improve the manuscript and these are gratefully acknowledged. The first author would like to thank the United Kingdom Engineering and Physical Sciences Research Council (EPSRC) for providing the funding to support his doctoral study (EP/T517951/1 with project reference 2558593). Z.X. was financially supported by EPSRC, United Kingdom grant (EP/V040235/1), the Royal Society Newton Advanced Fellowship, United Kingdom (NAF/R1/201156) and International Exchanges Award, United Kingdom (IEC/NSFC/211143, IES/R2/202095), and Alexander von Humboldt Research Fellowship in Germany.

Data availability

Data will be made available on request.

References

[1] Harlow FH, Welch JE. Numerical calculation of time-dependent viscous incompressible flow of fluid with free surface. Phys Fluids 1965;8(12):2182–9.
[2] Hirt CW, Nichols BD. Volume of fluid (VOF) method for the dynamics of free boundaries. J Comput Phys 1981;39(1):201–25.
[3] Rider WJ, Kothe DB. Reconstructing volume tracking. J Comput Phys 1998;141(2):112–52.
[4] Unverdi SO, Tryggvason G. A front-tracking method for viscous, incompressible, multi-fluid flows. J Comput Phys 1992;100(1):25–37.
[5] Osher S, Sethian JA. Fronts propagating with curvature-dependent speed: Algorithms based on Hamilton-Jacobi formulations. J Comput Phys 1988;79(1):12–49.
[6] Sethian JA, Smereka P. Level set methods for fluid interfaces. Annu Rev Fluid Mech 2003;35(1):341–72.
[7] Anderson DM, McFadden GB, Wheeler AA. Diffuse-interface methods in fluid mechanics. Annu Rev Fluid Mech 1998;30(1):139–65.
[8] Monaghan JJ. Smoothed Particle Hydrodynamics. Annu Rev Astron Astrophys 1992;30(1):543–74.
[9] Scardovelli R, Zaleski S. Direct numerical simulation of free-surface and interfacial flow. Annu Rev Fluid Mech 1999;31(1):567–603.

[10] Ubbink O, Issa R. A method for capturing sharp fluid interfaces on arbitrary meshes. J Comput Phys 1999;153(1):26–50.
[11] Xie Z, Pavlidis D, Salinas P, Percival JR, Pain CC, Matar OK. A balanced-force control volume finite element method for interfacial flows with surface tension using adaptive anisotropic unstructured meshes. Comput & Fluids 2016;138:38–50.
[12] Rudman M. Volume-tracking methods for interfacial flow calculations. Internat J Numer Methods Fluids 1997;24(7):671–91.
[13] Dyadechko V, Shashkov M. Moment-of-fluid interface reconstruction. In: Los Alamos Report la-UR-05-7571. 2005, p. 49.
[14] Lemoine A, Glockner S, Breil J. Moment-of-fluid analytic reconstruction on 2D Cartesian grids. J Comput Phys 2017;328:131–9.
[15] Mukundan AA, Ménard T, de Motta JCB, Berlemont A. A hybrid moment of fluid–level set framework for simulating primary atomization. J Comput Phys 2022;451:110864.
[16] Hergibo P, Phillips TN, Xie Z. A moment-of-fluid method for resolving filamentary structures using a symmetric multi-material approach. J Comput Phys 2023;491:112401.
[17] Ye Z, Sussman M, Zhan Y, Zhao X. A decision-tree based moment-of-fluid (DTMOF) method in 3D rectangular hexahedrons. 2021, arXiv preprint arXiv:2108.02533.
[18] Cutforth M, Barton PT, Nikiforakis N. An efficient moment-of-fluid interface tracking method. Comput & Fluids 2021;224:104964.
[19] Hill RN, Shashkov M. The symmetric moment-of-fluid interface reconstruction algorithm. J Comput Phys 2013;249:180–4.
[20] Ahn HT, Shashkov M. Multi-material interface reconstruction on generalized polyhedral meshes. J Comput Phys 2007;226(2):2096–132.
[21] Dyadechko V, Shashkov M. Reconstruction of multi-material interfaces from moment data. J Comput Phys 2008;227(11):5361–84.
[22] Jemison M, Sussman M, Shashkov M. Filament capturing with the multimaterial moment-of-fluid method. J Comput Phys 2015;285:149–72.
[23] Xie Z, Pavlidis D, Percival JR, Gomes JL, Pain CC, Matar OK. Adaptive unstructured mesh modelling of multiphase flows. Int J Multiph Flow 2014;67:104–10.
[24] Xie Z, Stoesser T. A three-dimensional Cartesian cut-cell/volume-of-fluid method for two-phase flows with moving bodies. J Comput Phys 2020;416:109536.
[25] Tryggvason G. Numerical simulations of the Rayleigh-Taylor instability. J Comput Phys 1988;75(2):253–82.
[26] Ding H, Spelt PD, Shu C. Diffuse interface model for incompressible two-phase flows with large density ratios. J Comput Phys 2007;226(2):2078–95.
[27] Chirco L, Zaleski S. An edge-based interface-tracking method for multiphase flows. Internat J Numer Methods Fluids 2023;95:491–7.
[28] Ahn HT, Shashkov M, Christon MA. The moment-of-fluid method in action. Commun Numer Methods Eng 2009;25(10):1009–18.
[29] Jemison M, Loch E, Sussman M, Shashkov M, Arienti M, Ohta M, Wang Y. A coupled level set-moment of fluid method for incompressible two-phase flows. J Sci Comput 2013;54(2):454–91.
[30] Schofield SP, Christon MA, Dyadechko V, Garimella RV, Lowrie RB, Swartz BK. Multi-material incompressible flow simulation using the moment-of-fluid method. Internat J Numer Methods Fluids 2010;63(8):931–52.
[31] Islam A, Sussman M, Hu H, Lian Y. Simulation of drop impact on substrate with micro-wells. Phys Fluids 2022;34(6):062108.
[32] Li G, Lian Y, Sussman M. Simulations of gas-liquid two-phase jet flows using the moment of fluid method. In: Fluids engineering division summer meeting. 55560, American Society of Mechanical Engineers; 2013, V01CT17A014.
[33] Banerjee S, Lian Y, Liu Y, Sussman M. A new method for estimating bubble diameter at different gravity levels for nucleate pool boiling. J Heat Transfer 2022;144(2):021601.
[34] Ferziger JH, Peric M. Computational methods for fluid dynamics. Springer; 2002.
[35] Xie Z. Numerical modelling of breaking waves under the influence of wind (Ph.D. thesis), University of Leeds; 2010.
[36] Xie Z. An implicit Cartesian cut-cell method for incompressible viscous flows with complex geometries. Comput Methods Appl Mech Engrg 2022;399:115449.
[37] Xie Z, Lin P, Stoesser T. A conservative and consistent implicit Cartesian cut-cell method for moving geometries with reduced spurious pressure oscillations. J Comput Phys 2022;459:111124.
[38] Hergibo P, Liang Q, Phillips TN, Xie Z. A quadtree-based adaptive moment-of-fluid method for interface reconstruction with filaments. J Comput Phys 2024;499:112719.
[39] Martin JC, Moyce WJ, Martin J, Moyce W, Penney WG, Price A, Thornhill C. Part IV. An experimental study of the collapse of liquid columns on a rigid horizontal plane. Philos Trans R Soc Lond Ser A Math Phys Eng Sci 1952;244(882):312–24.
[40] Pavlidis D, Gomes JL, Xie Z, Percival JR, Pain CC, Matar OK. Compressive advection and multi-component methods for interface-capturing. Internat J Numer Methods Fluids 2016;80(4):256–82.
[41] Hysing S, Turek S, Kuzmin D, Parolini N, Burman E, Ganesan S, Tobiska L. Quantitative benchmark computations of two-dimensional bubble dynamics. Internat J Numer Methods Fluids 2009;60(11):1259–88.
[42] Doherty W, Phillips TN, Xie Z. A stabilised finite element framework for viscoelastic multiphase flows using a conservative level-set method. J Comput Phys 2023;477:111936.